Asian Journal of Chemistry; Vol. 37, No. 1 (2025), 203-214

ASIAN JOURNAL OF CHEMISTRY

https://doi.org/10.14233/ajchem.2025.32982

Microscopic Analysis of Cathinone Derivative 4-Fluoromethcathinone Hydrochloride using Density Functional Theory and its Mechanism of Interaction with Biogenic Amine Neurotransmitter

AKANSHA TYAGI, NAVNEETA KOHLI, VARSHA RANI and ANUJ KUMAR*

Department of Physics, Chaudhary Charan Singh University, Meerut-250004, India

*Corresponding author: E-mail: dranujkumarccsu@gmail.com

Received: 3 November 2024; *Accepted*: 18 December 2024; *Published online*: 31 December 2024; AJC-21869

Synthetic cathinones, a new psychoactive substance more commonly known as bath salts, are designer drugs that pose a considerable challenge for prevention and treatment. A large number of such cathinone derivatives have been synthesized recently and the market is flooded with such synthetic psychoactive cathinone derivatives. Considering the possibility for misuse and adverse impacts on human health, it is crucial to collect analytical data on the newly synthesized cathinone derivatives available in the market. Therefore, it is essential to understand the most accurate identification of these substances and to establish a more efficacious therapy mechanism. Herein, a cathinone derivative 4-fluoromethcathinone hydrochloride (FMPHC) has been investigated using density functional theory (DFT). Systematic theoretical analysis for the optimized geometry, FT-Raman, FT-IR spectra and molecular reactivity descriptors such as HOMO-LUMO and molecular electrostatic potential (MEP) of this cathinone derivative is reported. The intra- and inter-molecular interactions of FMPHC crystal were analyzed using NBO analysis and Hirshfeld surface analysis, respectively. *In silico* molecular docking between the FMPHC ligand and a biogenic amine neurotransmitter, the norepinephrine transporter (hNET) responsible for alertness, arousal, and pain sensation is conducted to understand the mechanism of interaction of the norepinephrine transporter (hNET) with FMPHC.

Keywords: Cathinone derivatives, DFT, NBO, Molecular docking, Norepinephrine transporter.

INTRODUCTION

Synthetic cathinones, a new psychoactive substance, more commonly known as bath salts, are designer drugs and are being used as recreational drugs [1]. These have chemical similarities with the molecule called cathinone, which is present in the khat plant produced in East Africa and southern Arabia. Cathinones were initially intended to be the active pharmaceutical ingredients of pharmaceutical products such as amfepramone, which was used as an appetite suppressant and pyrovalerone, which was used as an anti-fatigue medication [2], but their abusive use as substitutes for traditional drugs is still a problem and poses a serious threat to public health. Numerous cathinone compounds are offered in the market under a broad range of brand names, both online and in drug accessory shops. A large number of cathinone derivatives have been synthesized recently [3,4], however, these derivatives can cause states of heightened excitement, elevated assertiveness, euphoria, greater focus, anxiety or restlessness. Abusing cathinone derivatives over an extended period can have negative effects on the nervous and circulatory systems, which can lead to permanent mental issues [5].

Synthetic cathinones develop a broad range of effects on awareness, excitement and perception of pain by interfering with the biogenic amines like norepinephrine, dopamine and serotonin neurotransmitters, whose levels in brain synapses are regulated by their corresponding transporters [6-8]. Cathinones, being stimulants, often act as substrate-type ligands for these transporters, meaning they are recognized by the transporter and taken up into the neuron. Both dopamine transporter (DAT) and serotonin transporter (SERT) are the integral membrane proteins located on the membrane of presynaptic neuron. Once inside, cathinones can inhibit the reuptake of neurotransmitters leading to increased levels of dopamine and serotonin in the synaptic cleft. Similarly, norepinephrine transporter (NET) is the target of various drugs, including certain antidepressants and psychostimulants. Inhibitors of NET, such as selective

serotonin-norepinephrine reuptake inhibitors (SNRIs) and tricyclic antidepressants (TCAs), increase the concentration of norepinephrine and other neurotransmitters in the synaptic cleft, which can improve symptoms of depression and other mood disorders [9]. All these psychoactive drugs disrupt the normal function of the brain by interacting with receptors of neurotransmitters that are present in the brain. There is still a lot to learn about how synthetic cathinones influence the human brain, even though numerous studies [10] have shown that they resemble stimulants like amphetamines, cocaine and MDMA.

In order to understand more about cathinone derivatives, Rojkiewicz *et al.* [11] identified and characterized two cathinone derivatives *viz*. 4-fluoro-methcathinone hydrochloride (FMPHC) and 1-(4-methylphenyl)-2-(ethylamino)pentan-1-one hydrochloride (MEAP), which are available in the market. In an attempt to further increase knowledge on cathinones derivatives at the molecular level, in the present study, we report comprehensive computational investigations on one of the cathinone derivatives, 4-fluoromethcathinone hydrochloride (FMPHC) [11] using density functional theory (DFT) and docking study. In order to get better insight into various properties at the molecular level, we have performed a systematic theoretical analysis of the results based on quantum chemical calculations for the optimized molecular structure, FT-IR and FT-Raman spectra, molecular electrostatic potential (MEP) and molecular reactivity descriptors derived from HOMO-LUMO of the cathinone derivative FMPHC. The intra- and inter-molecular interactions of FMPHC crystal were analyzed using NBO and Hirshfeld surface analysis, respectively. Understanding the interaction between cathinones and the NET transporter is crucial for understanding their pharmacological effects and potential abuse. To understand the inhibition effect of title molecule FMPHC on a biogenic amine neurotransmitter, the norepinephrine transporter (hNET), which affects pain perception, arousal and alertness in a variety of ways, *in silico* molecular docking studies are also being reported. Docking results will help in both, understanding the interaction mechanism at the molecular level and possible therupatic applications of the title molecules.

EXPERIMENTAL

Synthetic cathinones are related to the parent compound cathinone, which is found in khat plant and can be synthetically produced from propiophenone through a Friedel-Crafts acylation of propionic acid and benzene. Ring-substituted cathinone derivatives are claimed to have effects similar to those of cocaine, amphetamine or MDMA (ecstasy), but little is known of their detailed pharmacology [12]. A possible structure of cathinone derivative giving possible substitution sites is shown below:

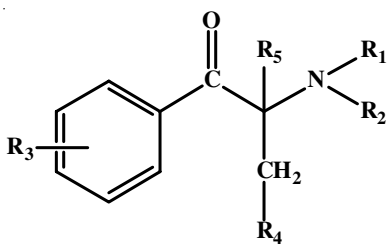

4-Fluoromethcathinone (4-FMC)hydrochloride (FMPHC) is available in the market and till date only physico-chemical characterization such as electrospray ionization ion trap mass spectrometry (MS), infrared, Raman, ultraviolet-visible spectroscopies, X-ray crystallography and nuclear magnetic resonance spectroscopy, is reported by Rojkiewicz *et al.* [11]. To further characterize FMPHC at the electronic level and to collect useful analytical data, GAUSSIAN-09 software tool are used [13] for the theoretical computations utilizing the B3LYP [14] hybrid exchange-correlation functional and 6-311++G (d,p) basis set. Gaussview05 [15] was used to visualize the optimized structure and frontier orbitals. Using the GAR2PED program [16], which was used to construct the internal coordinates for the optimized molecular structure using Pulay's recommendations [17], the vibrational (IR and Raman) wavenumbers and potental energy distribution (PED) of various modes have been calculated. Using the NBO 5.0 Program, the natural bond orbital (NBO) computations were carried out. Crystal Explorer 17.5 [18] was used to construct the Hirshfeld surface mapped over shape-index, curvedness, d_{norm} and fragment patch. The X-ray data CIF file served as the source for the initial geometry [11]. The contact distances from the Hirshfeld surface to the nearest atom inside and outside, respectively, are represented by the distances d_i and d_e, which stand for the two-dimensional fingerprint plots for various intermolecular interactions. To quantify the binding energy and the interaction of the ligand with target protein 6M0F, Auto dock Vina [19] has been used in molecular docking investigations. The programs Pymol [20] and discovery studio [21] were used to examine the docking data.

RESULTS AND DISCUSSION

Optimized geometry: 4-Fluoromethcathinone (4-FMC) hydrochloride was optimized with B3LYP functional and 6-311++G(d,p) basis set. The input coordinates for optimization were taken from the crystal information file: cif*. The optimized structure of the title compound with a numbering scheme is shown in Fig. 1. A comparison of the optimized structure parameters, such as bond lengths, bond angles and dihedral angles, with their experimental values [11] is given in Table-1.

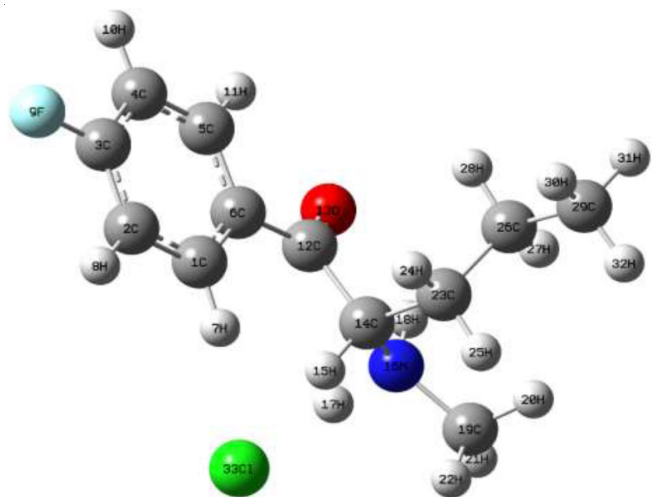

Fig. 1. Optimized molecular structure of FMPHC at B3LYP/6-311++G(d,p) level

TABLE-1
OPTIMIZED GEOMETRICAL PARAMETERS OF TITLE COMPOUND COMPARED WITH EXPERIMENTAL VALUES

Bond length

Geometrical parameters	Experimental values (Å) [Ref. 9]	Optimized values (Å) B3LYP/6-311 + + G(d,p)	Geometrical parameters	Experimental values (Å) [Ref. 9]	Optimized values (Å) B3LYP/6-311 + + G(d,p)	Geometrical parameters	Experimental values (Å) [Ref. 9]	Optimized values (Å) B3LYP/6-311 + + G(d,p)
C1-C2	1.39	1.39	C6-C12	1.49	1.48	C26-H28	0.99	1.09
C2-C3	1.38	1.39	C12-O13	1.09	1.22	C23-H24	0.99	1.10
C3-C4	1.38	1.39	C12-C14	1.53	1.54	C23-H25	0.99	1.10
C4-C5	1.39	1.39	C14-H15	0.99	1.09	C14-N16	1.50	1.49
C5-C6	1.40	1.41	C14-C23	1.54	1.54	N16-H17	0.91	1.14
C6-C1	1.40	1.40	C23-C26	1.53	1.54	N16-H18	0.91	1.02
C1-H7	0.95	1.08	C26-C29	1.53	1.53	N16-Cl33	4.12	2.86
C2-H8	0.95	1.08	C29-H32	0.98	1.09	N16-C19	1.49	1.48
C3-F9	1.36	1.35	C29-H30	0.98	1.09	C19-H20	0.98	1.09
C4-H10	0.95	1.35	C29-H31	0.98	1.09	C19-H21	0.98	1.09
C5-H11	0.95	1.08	C26-H27	0.99	1.10	C19-H22	0.98	1.09

Bond angles

Geometrical parameters	Experimental values (°)	Optimized values (°) B3LYP/6-311 + + G(d,p)	Geometrical parameters	Experimental values (°)	Optimized values (°) B3LYP/6-311 + + G(d,p)	Geometrical parameters	Experimental values (°)	Optimized values (°) B3LYP/6-311 + + G(d,p)
C1-C2-C3	118.36	118.52	C12-C6-C5	118.31	118.16	C14-C23-C26	114.69	116.99
C2-C3-C4	123.27	122.67	C6-C12-013	121.93	122.25	C14-C23-H25	108.56	108.17
C3-C4-C5	118.08	118.29	C6-C12-C14	117.75	119.33	C23-C26-H28	109.20	109.96
C4-C5-C6	120.55	120.69	013-C12-C14	120.30	118.26	H27-C26-H28	107.90	105.7
C5-C6-C1	119.53	119.40	C19-N16-H18	108.83	112.57	C23-C26-C29	112.10	111.86
C6-C1-C2	120.19	120.40	C19-N16-H17	108.78	106.29	H27-C26-C29	109.18	109.20
H7-C1-C2	119.89	118.88	N16-C19-H21	109.48	107.82	H28-C26-C29	109.19	109.67
H7-C1-C6	119.92	120.60	N16-C19-H20	109.45	111.71	C26-C29-H32	109.46	111.49
H8-C2-C1	120.79	121.60	N16-C19-H22	109.49	108.50	C26-C29-H30	109.48	111.14
H8-C2-C3	120.85	119.87	H15-C14-N16	108.47	105.03	H30-C29-H32	109.44	107.61
F9-C3-C2	118.30	118.75	C12-C14-C23	110.14	110.46	H32-C29-H31	109.48	107.69
F9-C3-C4	118.43	118.58	C12-C14-H15	110.68	110.60	C26-C29-H31	109.48	111.05
H10-C4-C3	120.93	119.80	H15-C14-C23	107.85	109.09	C14-N16-C19	113.76	117.86
H10-C4-C5	120.99	121.91	N16-C14C23	112.85	115.43	C14-N16-H18	108.82	108.13
H11-C5-C4	119.73	120.39	C14-C23-H24	108.58	106.53	C14-N16-H17	108.83	103.12
H11-C5-C6	119.72	118.92	H24-C23H25	107.57	105.36	H21-C19-H22	109.47	108.35
C12-C6-C1	122.11	122.39	H25-C23-C26	108.61	109.82	H21-C19-H20	109.45	109.90

Torsions angles

Geometrical parameters	Experimental values (°)	Optimized values (°) B3LYP/6-311 + + G(d,p)	Geometrical parameters	Experimental values (°)	Optimized values (°) B3LYP/6-311 + + G(d,p)	Geometrical parameters	Experimental values (°)	Optimized values (°) B3LYP/6-311 + + G(d,p)
C6-C1-C2-C3	-0.17	-0.56	H7-C1-C2-C3	179.82	-176.62	H18-N16-C19-H21	-64.59	-58.77
C1-C2-C3-C4	-0.49	1.15	H8-C2-C3-C4	179.52	-177.87	H17-N16-C19-H22	-67.59	-56.55
C2-C3-C4-C5	0.47	-0.21	F9-C3-C4-C5	-179.76	-179.72	H15-C14-C23-C26	177.52	179.41
C3-C4-C5-C6	0.22	-1.29	H10-C4-C5-C6	-179.79	179.19	C14-C23-C26-C29	175.98	-179.49
C4-C5-C6-C1	-0.85	1.81	H11-C5-C6-C1	179.11	-178.28	C23-C26-C29-H31	178.94	-179.87
C5-C6-C1-C2	0.82	-0.84	C12-C6-C1-C2	-176.85	-178.28	H24-C23-C26-H28	-66.81	-62.71
C12-C6-C1-H7	3.16	-2.33	C1-C6-C12-O13	163.75	153.25	H25-C23-C26-H27	58.72	65.99
H7-C1-C2-H8	-0.19	2.38	C1-C6-C12-C14	-18.12	-31.38	H28-C26-C29-H30	60.11	62.26
H8-C2-C3-F9	-0.26	1.64	O13-C12-C14-N16	-28.82	-36.63	H27-C26-C29-H32	-62.19	-62.28
F9-C3-C4-H10	0.25	-0.18	O13-C12-C14-H15	-146.11	-149.99	C12-C14-C23-H24	58.03	63.73
H10-C4-C5 H11	0.25	-0.73	C12-C14-N16-C19	-170.83	166.04	N16-C14-C23-H25	-64.31	-63.13
H11-C5-C6-C12	-3.13	-0.73	C14-N16-C19-H21	173.91	174.30	C5-C6-C12-O13	-13.95	-24.22

The title molecule mainly consists of one aromatic ring, an aliphatic chain and a carbonyl group. C-C and C-H bond lengths of florine substituted aromatic ring show their values in the characteristic range. Similarly, structural parameters of an aliphatic chain and a carbonyl group also have values similar to other compounds. Most of the theoretical bond lengths, bond angles and torsions are satisfactorily matching with the experimental data. Due to an isolated molecule model chosen for theoretical calculation, deviations in calculated values of few structural parameters are observed. For example, C2-H8, C4-H10, C12-O13, N16-H17 and N16-Cl33 bond lengths show significant differences in their theoretical and experimental values. N16-H17 and N16-Cl33 bond lengths show the maximum difference between theoretical and calculated values as these atoms are involved in the formation of coordinate bonds and are severely affected by inter-molecular interactions. These bonds are calculated at 1.14 Å and 2.86 Å while their experimental values are observed at 0.91 Å and 4.12 Å, respectively. Crystal packing effect caused by the presence of oxygen atom is responsible for about 10º deviation between experimental and theoretical values for C1-C6-C12-O13, C1-C6-C12-C14 and O13-C12-C14-N16 torsions.

Molecular electrostatic potential (MEP): The molecular electrostatic potential (MEP), provides a visual method that helps in identifying the nucleophilic and electrophilic sites on the molecule. Nucleophilic and electrophilic regions are the most favourable sites for the formation of interactions between drug molecules and receptors. MEP surface can also be used as an important tool in the study of new drugs [22]. The electrostatic potential map of FMPHC, shown in Fig. 2, illustrates the charge distributions of the molecule three-dimensionally. The hottest shades (tending to red) indicate negative values of electrostatic potential regions rich in electrons while blue shades indicate positive potential regions having electron deficiency. Different hues reflect different values of the electrostatic potential at the surface; red represents the most electronegative electrostatic potential, blue represents the most positive electrostatic potential and green represents zero potential. Potential increases in the order red < orange < yellow < green < blue. The colour

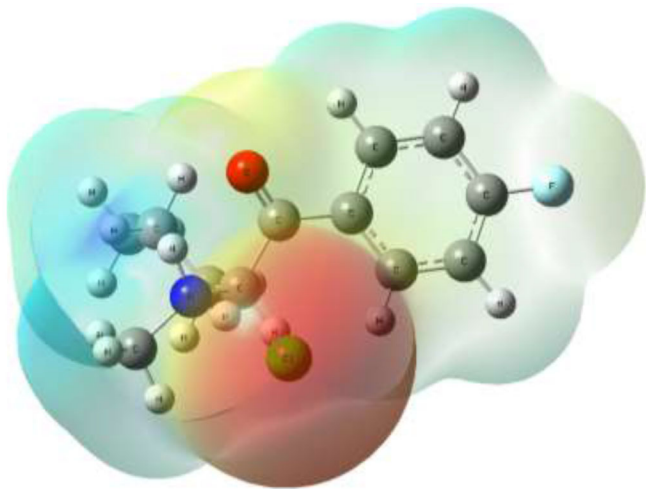

Fig. 2. Molecular electrostatic potential mapped on the isodensity surface for FMPHC molecule calculated at the B3LYP/6-311þþG(d,p) level of theory

code of this map is in the range -0.0676 a.u. (deepest red) to +0.0581 a.u. (deep blue). From Fig. 2, the MEP map shows that the most negative potential site lies over Cl33 atom, the orange region exists over O13 atom, while the region around N16, represented by blue, has the highest positive potential. Similarly, the aliphatic and aromatic hydrogens show moderate positive potential. Negative and positive sites are respectively susceptible to electrophilic and nucleophilic attack.

Frontier orbital analysis: The highest occupied molecular orbital (HOMO) and lowest unoccupied molecular orbital (LUMO) are the frontier orbitals that are crucial in determining the chemical stability and the reactivity of the species [23]. From the HOMO- LUMO plots of FMPHC molecule, shown in Fig. 3, it can be easily seen that during HOMO-LUMO transition, an isodensity shifting takes place from Cl atom to the ring and carbonyl group region. The values for HOMO, LUMO and band gap (HOMO-LUMO) have been calculated as -6.318 eV, -2.432 eV and 3.886 eV, respectively. The energy of HOMO and LUMO and their neighboring orbitals are all negative, which indicates that the optimized molecule is stable [24]. Global

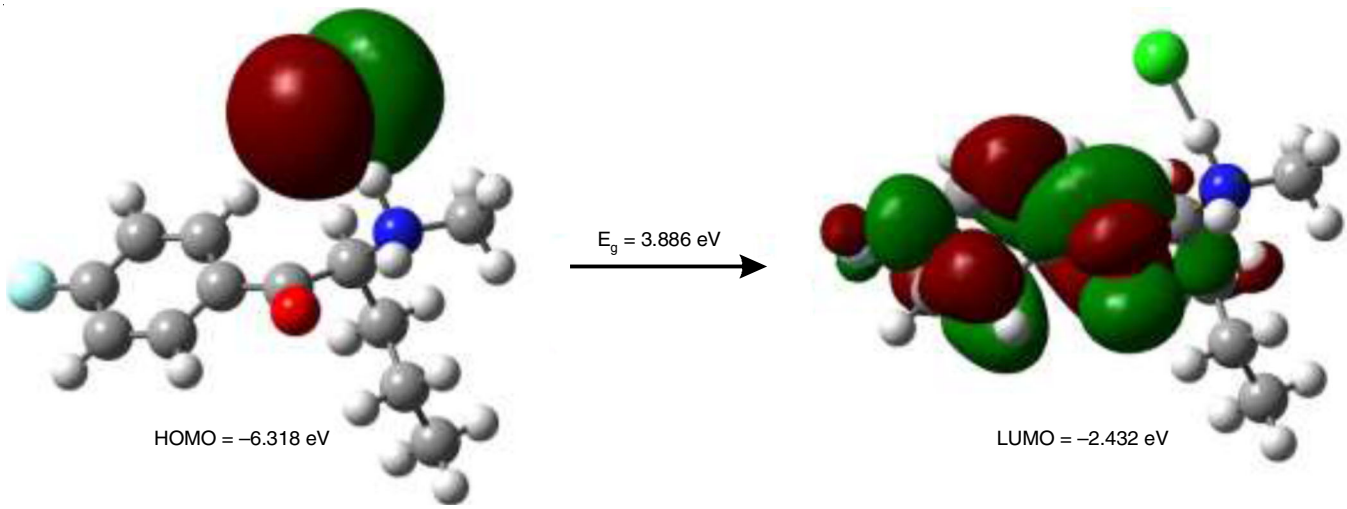

Fig. 3. Frontier molecular orbitals of FMPHC molecule

reactivity descriptors of FMPHC such as electronegativity (χ), chemical potential (μ), global hardness (η), global softness (S) and global electrophilicity index (ω); which describe the electrophilic behavior, have been calculated using HOMO-LUMO energies using eqns.: $\chi = -1/2(\varepsilon_{LUMO} + \varepsilon_{HOMO}) = 4.375$ eV; $\mu = -\chi = -1/2(\varepsilon_{LUMO} + \varepsilon_{HOMO}) = -4.375$ eV; $\eta = 1/2(\varepsilon_{LUMO} - \varepsilon_{HOMO}) = 1.943$ eV; $S = 1/2\eta = 0.025733402$ $(eV)^{-1}$; $\omega = \mu^2/2\eta = 4.9255339$ eV.

Vibrational spectra analysis: The 33 atoms in the FMPHC can produce 93 (3N-6) vibrational modes. Complete vibrational analysis in the DFT framework is done using B3LYP/6-311++G(d,p) basis set. Since anharmonicity was not taken into consideration by the Gaussian 09 program while computing wavenumbers, the harmonic vibrational wavenumbers of optimized structure were reduced by a factor of 0.944. The scaled and experimental FTIR and Raman spectra are compared in Figs. 4 and 5, respectively. The unscaled and scaled wavenumbers compared with the experimental spectrum wavenumbers, simulated IR intensities and Raman activities along with potential energy distribution (PED) for each normal mode are given in Table-2. The N-H stretching vibrations generally give absorption bands at wavenumbers above 3100 cm^{-1} in the absence of intra- and inter-molecular hydrogen bond interactions [25]. The N-H stretching mode N16-H18 bond was calculated at 3242 cm^{-1}. This mode was observed in the FTIR spectrum at 3127 cm^{-1} and in the Raman spectrum at 3242 cm^{-1}. The other N16-H17 stretch, with H17 involved in ionic bonding, is highly coupled with δ(C17C14N16) + ν(H17Cl33) + δ(H17H18N16) vibrations and calculated at a much lower wavenumber equal to 1688 cm^{-1}. The presence of C-H stretching vibration in the region 3100-3000 cm^{-1} of the heteroaromatic structure, which is the distinctive region for the quick detection of C-H stretching vibration, is evident [26]. The CH stretching bands was calculated at 3030, 3028, 3017 and 3015 cm^{-1} and assigned to the observed broadband at 3045 cm^{-1} in FTIR spectrum and at 3031 cm^{-1} in the Raman spectrum. The identification of C-N vibrations is highly challenging due to the mixing of several bands. However, the C-N vibrations are assigned in this work using theoretical calculations. The C-N stretching mode is found to be responsible for the extremely low band at 1124 cm^{-1} in the FTIR spectrum. The C12O13 stretching belonging to the carbonyl group is calculated at 1633 cm^{-1} and assigned to observed peaks at 1600 cm^{-1} and 1634 cm^{-1} in IR and Raman spectra, respectively. Since the computed results and the vibrational spectra of the molecule explicitly provide information on functional groups as well as molecular conformation, computational methods in conjunction with vibrational spectra have been used as a key tool in the current study [27].

NBO analysis: The NBO analysis is an established method for evaluating a particular molecule's charge transfer properties and extent of intramolecular bonding. It is demonstrated *via* the second-order perturbation theory that some energy loss is connected to these effects. The strength of the delocalization is proportional to the stabilizing energy E(2) of each donor NBO(i) and acceptor NBO(j) group, which may be calculated using the following formula:

$$E(2) = -n_\sigma \left(\frac{\langle \sigma | F | \sigma \rangle^2}{\varepsilon_{\sigma^*} - \varepsilon_\sigma} \right) = -\eta_\sigma \left(\frac{F_{ij}^2}{\Delta E} \right)$$

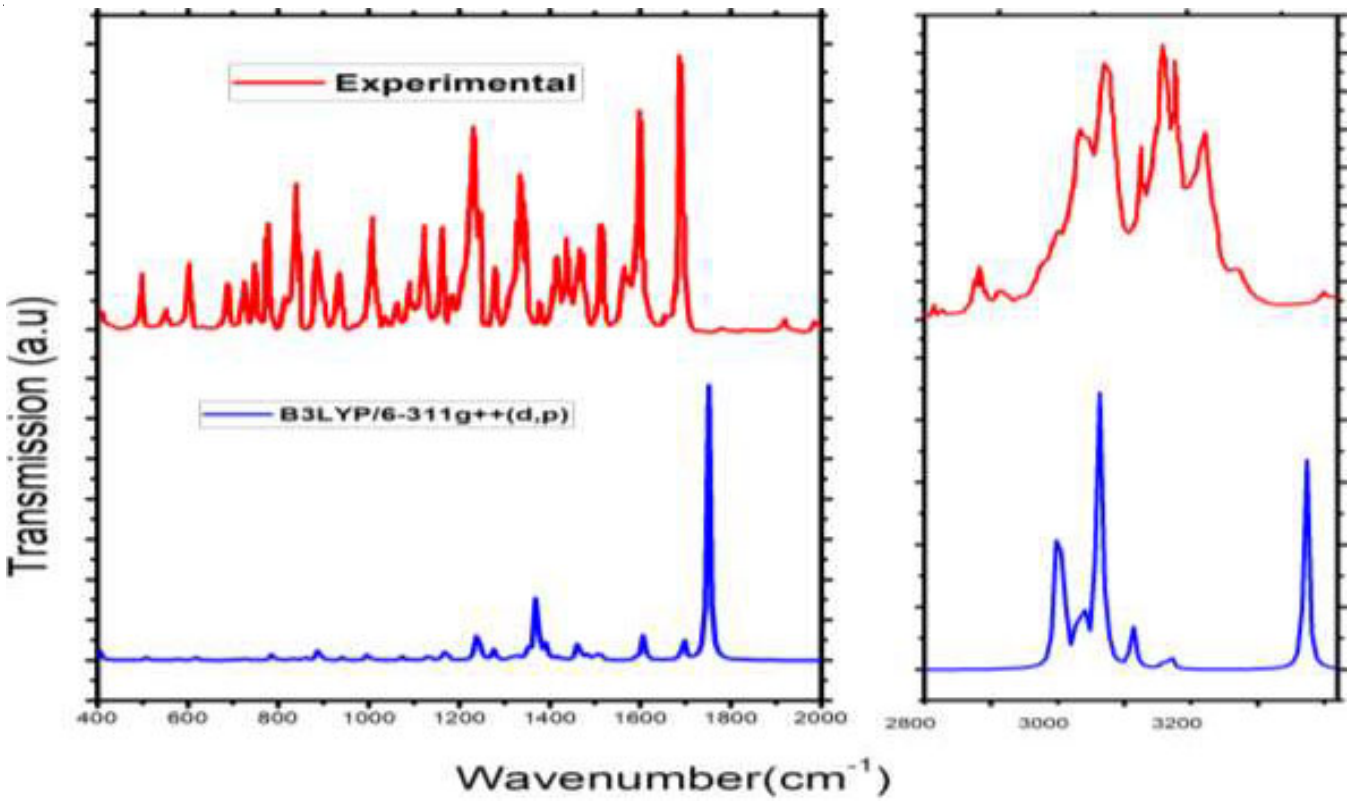

Fig. 4. Computational and experimental FTIR spectra of FMPHC

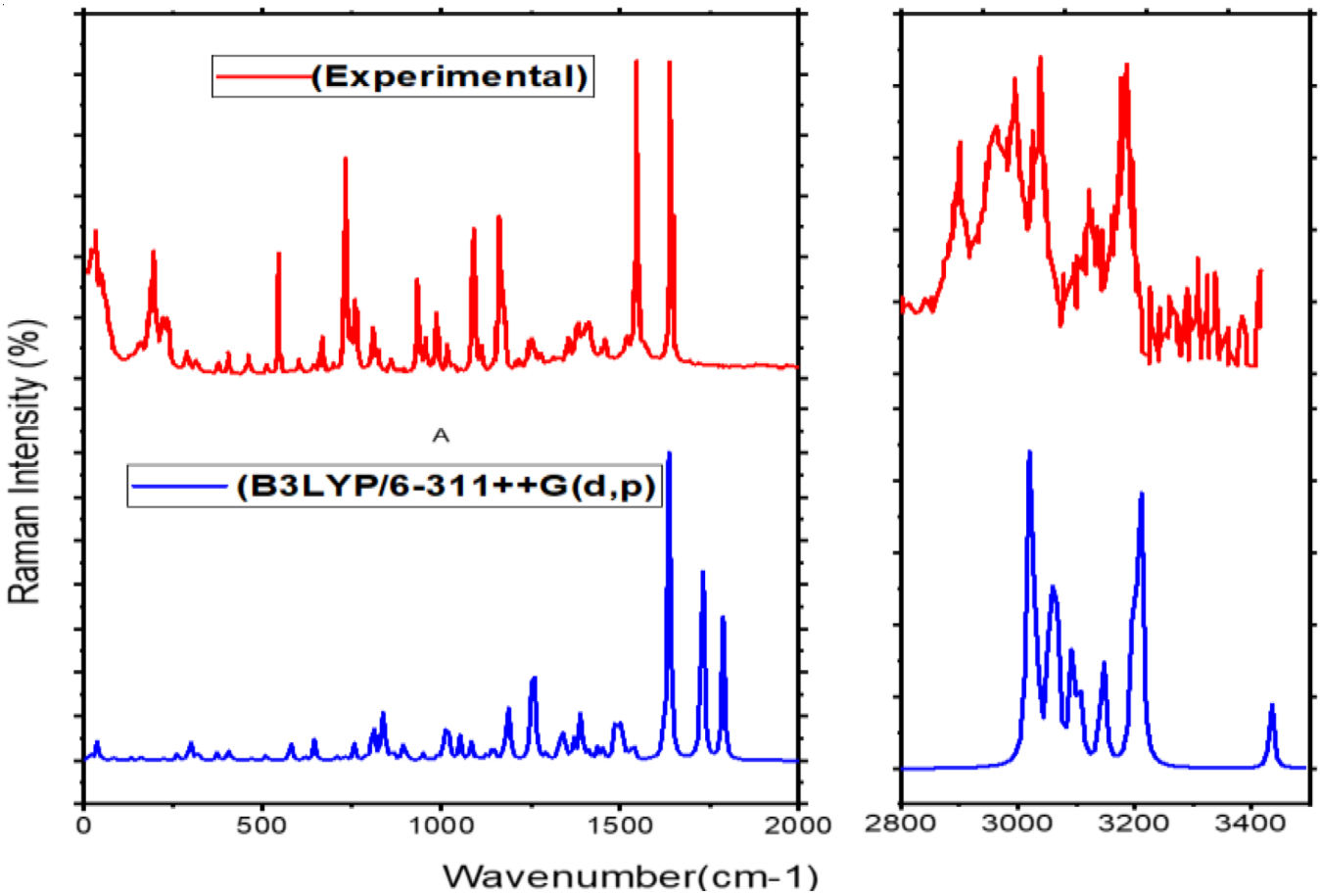

Fig. 5. Computational and experimental Raman spectra of FMPHC molecule

TABLE-2
VIBRATIONAL WAVENUMBERS, IR INTENSITIES AND RAMAN SCATTERING ACTIVITIES OF FMPHC ALONG WITH % POTENTIAL ENERGY DISTRIBUTION

Unscaled	Scaled	Calculated		Observed		Assignment (% PED, internal coordinates having contribution > 5%) are shown
		IR	Raman	IR	Raman	
3435	3242	53.4672	50.0342	3127	3242	ν(N16H18)(98)
3210	3030	2.108	182.3372	3045	3031	ν(C2H8)(71) + ν(C1H7)(29)
3208	3028	1.5155	114.8727		3023	ν(C4H10)(63) + ν(C5H11)(32)
3196	3017	0.6503	71.4698			ν(C1H7)(63) + ν(C2H8)(20) + ν(C5H11)(11)
3194	3015	0.5093	13.4355		3013	ν(C5H11)(54) + ν(C4H10)(29)
3149	2972	6.9223	35.7577	2974	2973	ν(C19H20)(54) + ν(C19H22)(45)
3145	2968	4.3699	66.1832	2969		ν(C19H21)(67) + ν(C19H22)(23) + ν(C19H20)(10)
3108	2934	2.0805	41.9155	2933	2939	ν(C14H15)(98)
3095	2922	28.5138	99.1429			ν(C29H31)(75) + ν(C29H30)(13) + ν(C29H32)(9)
3090	2917	60.3724	12.4439	2917	2917	ν(C29H30)(31) + ν(C26H28)(30) + ν(C29H32)(25) + ν(C26H27)(7)
3069	2897	4.554	22.5762			ν(C26H28)(38) + ν(C29H30)(21) + ν(C29H30)(19) + ν(C23H25)(13) + ν(C23H24)(12)
3064	2892	11.99	173.6923			ν(C19H20)(34) + ν(C19H22)(31) + ν(C19H21)(30)
3054	2883	7.9612	80.576	2885	2876	ν(C23H24)(43) + ν(C26H28)(29) + ν(C23H25)(24)
3031	2861	27.7676	100.6875			ν(C23H25)(54) + ν(C23H24)(30) + ν(C26H27)(11)
3022	2853	22.803	120.0735	2859		ν(C29H32)(42) + ν(C29H30)(33) + ν(C29H31)(20)
3018	2849	11.1144	144.9302		2837	ν(C26H27)(79) + ν(C23H24)(9) + ν(C26H28)(7)
1788	1688	1974.902	60.4584	1686		ν(N16H17)(63) + δ(C17C14N16)(13) + ν(H17Cl33) + δ(H17H18N16)
1730	1633	177.6798	103.4509	1600	1634	ν(C12O13)(83)
1637	1545	188.4988	134.7331	1564	1544	ν(C4H5)(21) + ν(C1H2)(20)
1622	1532	28.6084	10.0288	1515		ν(C2H3)(25) + ν(C3H4)(17) + ν(C5H6)(14) + ν(C1H6)(12)
1538	1452	43.1869	5.391	1466	1452	δ(C2H7C1)(14) + δ(C6H11C5)(11) + δ(C5H10C4)(11)
1528	1443	49.6252	4.1618	1442		τ(C14Cl33H17N16)(54) + τ(C14N16H17Cl33)(44)

1513	1428	7.3969	1.775			τ(C14Cl33H17N16)(46) + τ(C14N16H17Cl33)(39)
1508	1423	32.1744	4.8443			δ(H20H21C19)(44) + δ(H27H28C26)(17) + ρ(H3H32C29)(10) + δ(H21N16C19)(6) + τ(C14Cl33H17N16)(6)
1501	1417	9.474	8.5695	1417		δ(H30H31C29)(35) + τ(C14Cl33H17N16)(30) + τ(C19N16H17Cl33)(23)
1496	1412	1.8548	6.8806			τ(C14Cl33H17N16)(50) + τ(C19N16H17Cl33)(40)
1491	1407	20.2233	5.0317			τ(C14Cl33H17N16)(49) + τ(C19N16H17Cl33)(38)
1486	1403	113.5715	5.7189			ω(Cl33C14N16)(24) + δ(H20H21C19)(22) + τ(C19H17H18N16)(11) + sci(H17H18N16)(6)
1485	1401	14.6432	6.7538			τ(C14Cl33H17N16)(40) + τ(C19N16H17Cl33)(39) + δ(H24H25C23)(13)
1453	1371	7.4708	3.9867	1381	1384	τ(C19N16H17Cl33)(44) + τ(C14Cl33H17N16)(32) + δ(H20H21C19)(6)
1438	1357	26.9805	5.4497		1351	ν(C1C2)(16) + ν(C4C5)(15) + τ(C19N16H17Cl33)(12) + δ(C3H8C2)(8) + τ(C14Cl33H17N16)(7) + δ(C5H10C4)(6) + δ(H20H21C19)(6) + δ(C2H7C1)(6)
1417	1338	8.4918	0.5584			δ(H30H31C29)(75) + δ(C14H24C23)(6)
1410	1331	121.8995	3.3371	1334		δ(C14C24C23)(17) + δ(C23H27C26)(13) + τ(C19N16H17Cl33) + τ(C14Cl33H17N16)(12) + δ(H30H31C29)(7) + δ(Cl33C14N16)(7) + δ(H20H21C19)(7)
1390	1312	562.8948	22.2547		1312	τ(C19N16H17Cl33)(30) + τ(C14Cl33H17N16)(29) + δ(Cl33C14N16)(12) + ν(N16H17)(8)
1370	1294	80.299	8.7331			τ(C19N16H17Cl33)(42) + τ(C14Cl33H17N16)(32)
1349	1273	22.6481	3.2295			δ(C23H27C26)(27) + δ(H15C23C14)(25) + τ(C19N16H17Cl33)(9) + δ(C14C24C23)(7) + τ(C14Cl33H17N16)(6)
1340	1265	4.4734	3.2525	1338		ν(C5C6)(18) + ν(C1C6)(18) + ν(C2C3)(17) + ν(C3C4)(15) + ν(C4C5)(8) + ν(C1C2)(6) + δ(C6C12O13)(6)
1336	1261	29.4608	12.1883	1277		τ(C14Cl33H17N16)(28) +(C19N16H17Cl33)(27) + δ(C23H27C26)(22) + δ(C14C24C23)(9)
1326	1251	4.7246	2.1437	1250	1248	δ(C2H7C1)(29) + δ(C6H11C5)(20) + δ(C5C19C4)(15) + δ(C3H8C2)(14)
1294	1221	89.2624	2.4609			τ(C14Cl33H17N16)(25) + γ(C19N16H17Cl33)(24) + δ(C14H24C23)(10)
1263	1193	41.7018	4.1744			δ(C14H24C23)(28) + δ(C23H27C26)(10) + δ(C23H27C26)(8) + δ(H15C12C14)(8) + δ(H30C26C29)(6)
1260	1189	63.9833	24.1137	1186		δ(C6C12O13)(21) + ν(C6C12)(20) + δ(C14O13C12)(15) + δ(C6C2C1)(7) + δ(H15C12C14)(6)
1252	1182	155.9236	24.0632	1158		ν(C3F9)(41) + ν(C1C2)(10) + δ(C6H11C5)(7) + ν(C4C5)(7)
1190	1123	5.9335	17.9546	1122		τ(C14Cl33H17N16)(28) + δ(H21N16C19)(24) + ν(C14N16)(8) + δ(H15C12C14)(6)
1184	1118	59.6943	5.0718			δ(C3H8C2)(17) + δ(H20N16C19)(16) + δ(C5C19C4)(9)
1178	1112	37.1305	6.2316			δ(H20N16C19)(19) + τ(C14Cl33H17N16)(17) + τ(C19N16H17Cl33)(14) + δ(C3H8C2)(7)
1144	1080	44.2032	6.7798	1085	1088	τ(C19N16H17Cl33)(27) + τ(C14Cl33H17N16)(22) + δ(C14H24C23)(8) + δ(C23H27C26)(6)
1126	1063	2.9952	1.9482	1058		δ(C5C19C4)(17) + δ(C3H8C2)(14) + δ(C6H11C5)(12) + ν(C1C2)(11) + ν(C4C5)(10) + τ(C19N16H17Cl33)(7) + δ(C2H7C1)(6)
1104	1042	3.7454	1.2322			τ(C19N16H17Cl33)(30) + τ(C14Cl33H17N16)(27) + ρ(H31C26C29)(10) + ν(C23C26)(8)
1083	1022	29.874	6.9069		1022	ν(N16C19)(34) + ν(C14N16)(20) + ν(C14C23)(14) + OUT(C14Cl33H17N16)(6)
1052	993	1.1167	8.7351		981	ν(C26C29)(24) + ν(N16C19)(16) + τ(C14Cl33H17N16)(13) + τ(C19N16H17Cl33)(12) + ν(C23C26)(8)
1030	972	1.744	0.3738			δ(C6C2C1)(33) + ν(C5C6)(11) + ν(C2C3)(9) + ν(C3C4)(9) + ν(C1C6)(8) + δ(C5C19C4)(6)
1016	959	10.2459	19.302		956	τ(C14Cl33H17N16)(18) + τ(C19N16H17Cl33)(16) + ν(C26C29)(13) + δ(C14C12O13)(11) + δ(C6C12O13)(6)
1006	950	43.1747	3.4048	1003		δ(C14C12O13)(20) + δ(C6C12O13)(17) + τ(C19N16H17Cl33)(11) + ν(C12C14)(10) + OUT(C14Cl33H17N16)(10)
988	933	0.683	1.1299	933	933	τ(H11C6C4C5)(47) + τ(H10C5C3C4)(25) + τ(H7C2C6C1)(9) + δ(H8C3C1C2)(7)
969	915	0.0567	0.2794			τ(H7C2C6C1)(37) + τ(H8C3C1C2)(24) + τ(C6C1C2C3)(16) + τ(H11C6C4C5)(10)
949	896	23.7257	2.4284	887		τ(C14Cl33H17N16)(48) + τ(C19N16H17Cl33)(44)
902	852	11.1974	1.5933		859	τ(C14Cl33H17N16)(26) + τ(C19N16H17Cl33)(24) + ρ(H31C26C29)(8) + δ(C14H24C23)(7) + δ(C14C12O13)(6)
894	844	83.291	5.9949	835		τ(C14Cl33H17N16)(45) + τ(C19N16H17Cl33)(40)

865	816	26.6973	3.5411	813	807	τ(H10C5C3C4)(22) + τ(H8C3C1C2)(12) + τ(H11C6C4C5)(9) + δ(C4F9C3)(9) + τ(C14Cl33H17N16)(7) + γ(H7C2C6C1)(7) + τasy(C19N16H17Cl33)(7)
838	791	13.397	19.5012		796	ν(C3F9)(12) + δ(C1C3C2)(10) + ν(C3C4)(7) + ν(C2C3)(7) + τ(C14Cl33H17N16)(6) + δ(H30C26C29)(6)
830	783	0.6902	2.3634			τ(H8C3C1C2)(33) + τ(H10C5C3C4)(25) + τ(H7C2C6C1)(23) + τ(H11C6C4C5)(14)
809	763	5.5177	16.7252	769	763	ν(C14N16)(19) + δ(C6C12O13)(12) + ν(C14N23)(10) + δ(C14O13C12)(7) + δ(H30C26C29)(6)
789	745	47.3654	0.8358	744		OUT(O13C14C6C12)(13) + OUT(C14Cl33H17N16)(13) + τ(C19N16H17Cl33)(11) + Γ(C6C1C2C3)(7) + δ(C14O13C12)(6) + δ(C12C23C14)(6)
756	714	2.2437	5.4433	719	729	τ(C6C1C2C3)(23) + δ(C23H27C26)(7) + τ(C12C5C1C6)(7) + δ(C4F9C3)(6) + τ(C19N16H17Cl33)(6)
729	688	14.2501	1.5211	686		δ(C23H27C26)(26) + δ(C14H24C23)(18) + τ(C14Cl33H17N16)(9) + τ(C19N16H17Cl33)(7)
706	666	8.4079	1.5302		665	τ(C6C1C2C3)(57) + δ(C4F9C3)(13)
644	608	1.6926	6.8461	604	603	δ(C5C1C6)(49) + δ(C1C3C2)(26)
618	583	27.1447	1.2684			δ(C14O13C12)(27) + δ(C6C12O13)(12) + δ(C5C1C6)(10) + ν(C6C12)(6)
578	545	14.1834	6.8305	552	540	δ(C6C12O13)(28) + δ(C14O13C12)(16) + ν(N16C14)(10)
510	481	23.0955	1.6932		459	δ(C4F9C3)(31) + τasy(C5C6C1C2)(25) + τ(C12C5C1C6)(11) + τasy(C2C3C4C5)(8)
471	444	0.1403	0.8223			δ(C6C12O13)(15) + δ(C1C3C2)(14) + δ(C1C12C6)(11) + δ(C4F9C3)(10) + OUT(C14Cl33H17N16)(8)
422	398	1.2543	0.3657		407	τ asy(C2C3C4C5)(62) + τasy(C5C6C1C2)(19)
406	383	65.0322	2.5781			τ(C14Cl33H17N16)(42) + τ(C19N16H17Cl33)(30) + ν(H17Cl33)(11)
400	378	36.5969	1.1721		374	δ(C4F9C3)(19) + OUT(C14Cl33H17N16)(16) + τ(C19N16H17Cl33)(16) + δ(C6C12O13)(11) + ν(H17Cl33)(9) + δ(C14O13C12)(6) + δ(C4F9C3)(6)
374	353	65.6186	2.5223			τ(C19N16H17Cl33)(41) + τ(C14Cl33H17N16)(27) + δ(C14O13C12)(8) + ν(H17Cl33)(6)
320	302	16.4197	2.9382		315	δ(C23N16C14)(10) + τ(C12C5C1C6)(8) + ν(H17Cl33)(8) + δ(C12N16C14)(8) + δ(C14O13C12)(7) + δ(C6C12O13)(6)
300	283	7.8148	5.0124		289	δ(H27H28C26)(27) + τ(C12C5C1C6)(11) + δ(C12C23C14)(8) + τasy(C5C6C1C2)(7) + ν(H17Cl33)(6) + δ(C6C1C2C3)(6)
291	274	3.5743	1.7047			δ(C14O13C12)(21) + τ(C19N16H17Cl33)(14) + δ(C12C23C14)(7) + δ(H27H28C26)(7)
261	246	4.6722	1.8606			τ(C14Cl33H17N16)(44) + τ(C19N16H17Cl33)(40)
229	216	2.4945	0.2353			τ(C14Cl33H17N16)(45) + τ(C19N16H17Cl33)(36) + τ(C23C26C29H30)(12)
219	207	3.4013	0.4553		200	τ(C14Cl33H17N16)(17) + δ(C1C12C6)(13) + δ(H24H25C23)(9) + τ(C19N16H17Cl33)(9) + δ(H27H28C26)(7)
202	190	8.0689	0.3431			τ(C14Cl33H17N16)(33) + τ(C14N16C19H20)(30) + τ(C19N16H17Cl33)(17)
166	157	0.5383	0.5422			τ(C19N16H17Cl33)(47) + τ(C14Cl33H17N16)(47)
158	149	10.0633	0.8529			τ(C19N16H17Cl33)(49) + τ(C14Cl33H17N16)(46)
132	124	2.1311	0.9093			τ(C19N16H17Cl33)(46) + τ(C14Cl33H17N16)(37)
112	105	1.3001	0.2049			τ(C19N16H17Cl33)(49) + τ(C14Cl33H17N16)(44)
82	77	0.8156	0.8125			τ(C19N16H17Cl33)(49) + τ(C14Cl33H17N16)(42)
73	69	1.4182	0.1157			τ(C19N16H17Cl33)(50) + τ(C14Cl33H17N16)(47)
55	52	6.8875	0.4662			τ(C19N16H17Cl33)(48) + τ(C14Cl33H17N16)(45)
38	36	6.3731	0.5844			τ(C14Cl33H17N16)(46) + τ(C19N16H17Cl33)(42)
37	35	0.6569	4.8076			τ(C1 C6C12O13)(40) + sci(Cl33H17N16)(12) + ω(Cl33C14N16)(10)
17	16	5.0075	2.3426			τ(C14Cl33H17N16)(38) + τ(C19N16H17Cl33)(34) + τ(C6C12C14H15)(8)

Types of vibration: δ-deformation (bending); ν-stretching; sci-scissoring; τ – torsion; ω-wagging; ρ-rocking.

where n_σ is the population of donor σ orbital and ε_{σ^*} and ε_σ are the energies of σ* and σ NBOs; $n_\sigma\langle|F|\sigma\rangle^2$ or F_{ij}^2 is the Fock matrix element, which corresponds to i^{th} and j^{th} NBO orbitals.

The FMPHC molecule contains nitrogen, oxygen and flourine (NOF) atoms which have high electronegativity. The high electron-withdrawing character of these atoms severely affects the charge distribution of the NBOs in the titled molecule. To be specific, natural bond orbitals of a lone pair LP*(1) on C3 with 99.99 % p character and 0.96306 electron density, a lone pair LP(1) on C4 with 99.98 % π character and 1.06744 electron density and a lone pair LP*(1) on H17 with 99.98 % σ character and 0.58990 electron density are present in Fock

matrix. Dominant donor-acceptor interactions along with their stabilization energies are given in Table-3. It can be observed that most of the dominant interactions are either n-π or n-n, while the hyperconjugative π-π* interaction which is responsible for electron delocalization along the chain in the molecule is missing. This is quite understandable in terms of the absence of ? bond in the main chain. The presence of F, N and O atoms having lone pairs is responsible for intra- and inter-molecular hydrogen bonding in the FMPHC molecule.

The important n-π interactions are electron transfer from n1*(C3) and n1(C6) lone pairs to antibonding π*(C1-C2) and π*(C4-C5), π*(C1-C2), π*(C4-C5) and π*(C12 -O13) with corresponding stabilization energies 53.81 and 52.02, 71.42, 68.86 and 53.53 kcal mol^{-1}, respectively. A reverse n-π electron transfer is observed from π(C1-C2) to n1*(C3) and n1(C6), π(C4 - C5) to n1*(C3) and n1(C6) and π(C12 -O13) to n1(C6) with stabilization energies equal to 66.35 and 43.8, 64.14 and 41.13 and 5.61 kcal mol^{-1}, respectively. These interactions show an electron transfer from the donor π bond to antibonding LP1* of C3 and bonding LP1 of C6 of the ring. A similar type of charge delocalization for the benzene ring in a similar environment was also observed previously [27]. These electron transfer interactions also have similar effects on ring bond character. As expected, atoms involved in, coordinate bonds (N16 and H17) and ionic bond (Cl33), show electron delocalization. The value of the highest stabilization energy of 305.01 kcal mol-1 is obtained for an interaction between n1(N16) and n1*(H17). A strong interaction between n4(Cl33) and n1*(H17) with stabilization energy equal to 167.80 kcal mol^{-1} is also observed. This interactions between N16, Cl33 lone pairs, with n1*(H17) weakens the N16-H17 bond resulting in the elongation of this bond. This is in agreement with the increased N16-H17 bond length of 1.14250 Å.

Hirshfeld surface analysis: The Hirshfeld surface analyses of FMPHC compound was done using the free Crystal Explorer 17.5 program [18]. The .cif file was used to calculate the surfaces and fingerprint plots. We can determine the intermolecular interactions and intermolecular contact sites inside the solid state packing of any chemical in crystalline form with the help of this technique. The close contact intermolecular interaction distances are the separations between potential interaction sites over the closed Hirshfeld surface of the primary molecule and potential interaction sites over other nearby molecular groups. Two distances, d_i and d_e, which separate the surface and the closest atoms on the inside and outside of the surface, respectively (shown in fingerprint plots) were determined using a normalized contact distance function (d_{norm}). The d_i, d_e and van der Walls radius of the concerned atom, which is in close contact with the surface, determine the normalized distance, d_{norm}, according to the following equation:

$$d_{norm} = \frac{d_i - r_i^{VdW}}{r_i^{VdW}} + \frac{d_e - r_e^{VdW}}{r_e^{VdW}}$$

here, the van der Waals radius of the d_e and d_i atoms is denoted as r_e^{VdW} and r_i^{VdW}, respectively [28].

In the 3D Hirshfeld surface (HS) map shown in Fig. 6, the white areas denote contacts close to the van der Waals separation, the blue spots denote longer contacts [29] in the d_{norm} surface and the dark red spots denote strong hydrogen bond locations on the crystal. Hirshfeld surfaces (HS) are mapped over d_{norm} (-0.4974 to 1.0591 Å), d_i (0.7848 to 2.3888 Å) and d_e (0.7859 to 2.4665 Å).

Shape index shows function depending on the HS flatness or curvature. On the Hirshfeld surface mapped with shape index function, one can notice red (pit) and blue (bump) portions which show the negative and positive locations for intermolecular

TABLE-3
SECOND-ORDER PERTURBATION THEORY ANALYSIS OF FOCK MATRIX IN NBO BASIS FOR FMPHC

Donor NBO(i)	ED(i)/e	Acceptor NBO(j)	ED(j)/e	$E^{(2)a}$ (kcal mol^{-1})	E(j)-E(i)[b] (a.u)	F(i,j)[c] (a.u)
πC1-C2	1.66331	n1* C3	0.96306	66.35	0.12	0.098
		n1 C6	1.06744	43.08	0.14	0.088
πC4-C5	1.67517	n1* C3	0.96306	64.14	0.13	0.097
		n 1 C6	1.06744	41.13	0.14	0.087
πC12-O13	1.97761	n 1 C6	1.06744	5.61	0.28	0.051
σC23-H24	1.97209	σ* C14-N 16	0.03252	5.40	0.78	0.058
n1* C3	0.96306	π* C1-C2	0.30787	53.81	0.16	0.104
		π* C4-C5	0.29275	52.02	0.16	0.103
n1 C6	1.06744	π* C1-C2	0.30787	71.42	0.14	0.108
		π* C4-C5	0.29275	68.86	0.14	0.107
		π* C12-O13	0.14376	53.53	0.13	0.096
n2 F9	1.97223	σ* C2-C3	0.02677	6.01	0.97	0.068
		σ* C3-C4	0.02727	6.02	0.97	0.068
n3 F9	1.91849	n1* C3	0.96306	31.61	0.28	0.112
n2 O13	1.88361	σ*C6-C12	0.06077	18.39	0.73	0.105
		σ*C12-C14	0.07013	20.18	0.63	0.102
σC14-N16	1.98480	n1* H17	0.58990	13.08	0.77	0.106
σN16-H18	1.98388	n1* H17	0.58990	10.03	0.69	0.088
σN16-C19	1.99126	n1* H17	0.58990	11.75	0.78	0.101
n1 N16	1.64522	n1* H17	0.58990	305.01	0.39	0.327
n1 Cl33	1.99862	n1* H17	0.58990	8.42	0.78	0.086
n4 Cl33	1.73932	n1* H17	0.58990	167.80	0.31	0.222

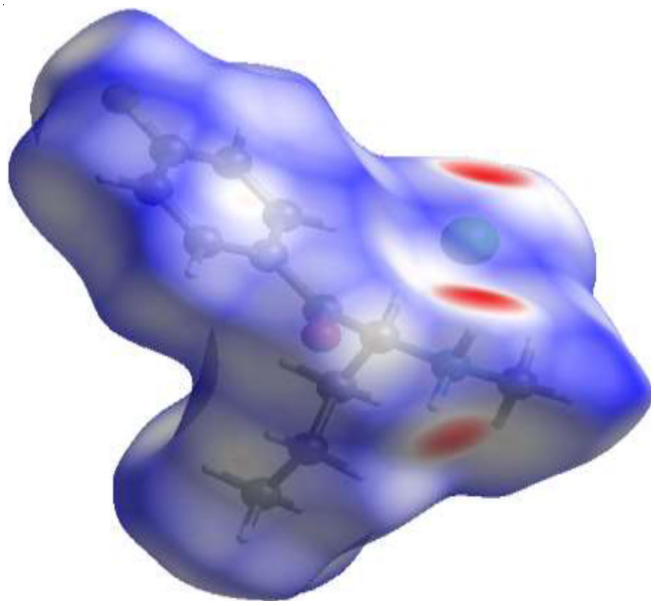

Fig. 6. Hirshfeld surface mapped over d_{norm} (-0.10000 to +1.0000 a.u.)

hydrogen bonding, respectively. The red regions corresponds to C–H···π interactions in Fig. 7a. It can be seen from Fig. 7b that there are many large green flat areas separated by blue edges in curvedness surface of molecule corresponding to high values of curvedness, which allows us to get information about interactions between neighboring molecules.The crystal typical packing modes are represented by shape index and curvature. These plots can also be used to determine whether stacking interactions, such as π-π and C-H···π are present. The shape index is mapped in the range -1.0000 to 1.0000 and curvedness in the -4.000 to 4.000 . The mapping colors patches in Fig. 7c allows us to identify the closest neighbour coordination environment of a molecule.

Identifying complementary places where one component performs as a hydrogen atom donor, represented by points with $d_e > d_i$ and the other as a hydrogen bond acceptor, indicated by points with $d_e < d_i$, can be done using the fingerprint plot (FP), which is shown in Fig. 8. The fingerprint plots in Fig. 8 clearly depict the respective contributions of the H···H, Cl···H/H···Cl, H···C/C···H, H···F/N···F and O···H/H···O contacts to the 3D d_{norm} Hirshfeld surface for the molecule. The main contribution of inter-contacts to the Hirshfeld surfaces are H-H (48.6%) and H-Cl/Cl-H (13.2%).

Molecular docking studies: The goal of ligand-protein docking is to predict the predominant binding mode(s) of a ligand with a protein having a known three-dimensional structure. A biogenic amine neurotransmitter, norepinephrine transporter (NET) has broad effects on alertness, arousal and pain perception [30]. Blocking norepinephrine absorption has become a critical component of the management of chronic pain and depression. The X-ray crystal structure of the human norepinephrine transporter (hNET) is not obtained yet and special structures resembling hNET are used for the study of inhibition activity by potent drug molecules. In this study, we have used the drosophila melanogaster dopamine transporter (6M0F), as the surrogate for human norepinephrine transporter (hNET) for molecular docking with the FMPHC ligand. The optimized structure of the FMPHC molecule using Gaussian 09 software was converted to PDB format using Avogadro software. Using the AutoDock Vina [19], the molecular docking simulation was performed in which docking is done on putative binding regions of the given protein. Using AutoDock software, the proteins were prepared for docking investigations. Polar hydrogen is added to protein structures. On the interdimeric enzyme surface, the binding modes are docked using grid box parameters of 50 × 50 × 50 Å, grid spacing of 0.435 Å and exhaustiveness = 9. The grid centers are kept at X = -4.170 Å, Y = 7.080 Å and Z = -5.764 Å. The binding position of the designated compound with the target proteins was examined by the molecular docking studies. FMPHC surrounded in the active pocket consisted of five amino acid residues LYS43, LYS104, TYR88, GLN39 and THR86 at the C terminus of the protein, shown in Fig. 9. Three hydrogen bonds are formed between the ligand FMPHC and the protein. Out of these three, the two hydrogen bonds are formed between the oxygen and TYR88, GLN39 residues having bond lengths equal to 3.16 Å and 2.84 Å, respectively. Another hydrogen bond is formed between the residue THR86 and carbon of bond length 1.99 Å. For the visualization of hydrogen bond interaction between the protein and ligand, Pymol [20] and Discovery Studio [21] softwares were used. Fig. 10 represents the protein-ligand interactions at the specific

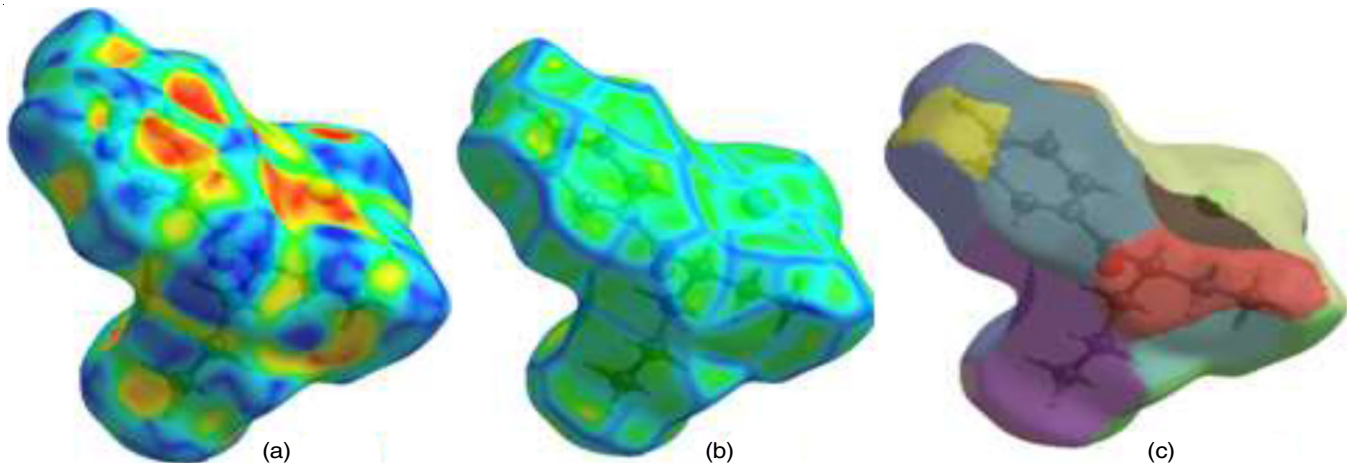

Fig. 7. Hirshfeld surface mapped with (a) shape index (b) curvedness (c) Fragment patch

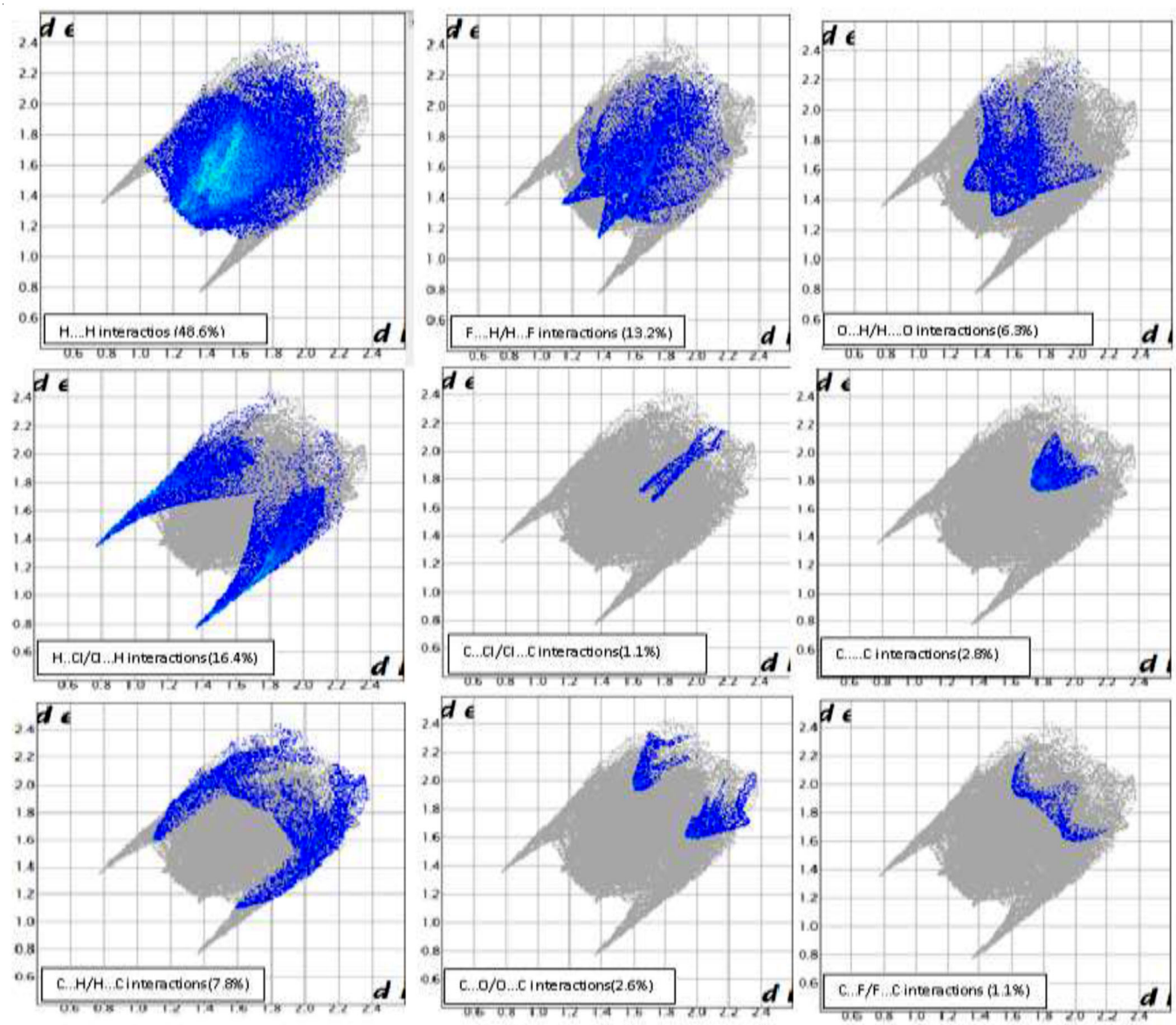

Fig. 8. Finger print plots of various interactions

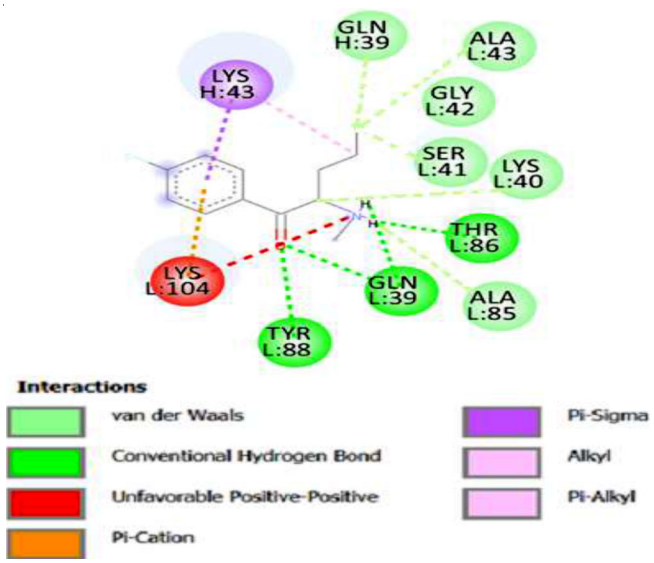

Fig. 9. Binding of FMPHC with 6M0F protein in the 2D diagram

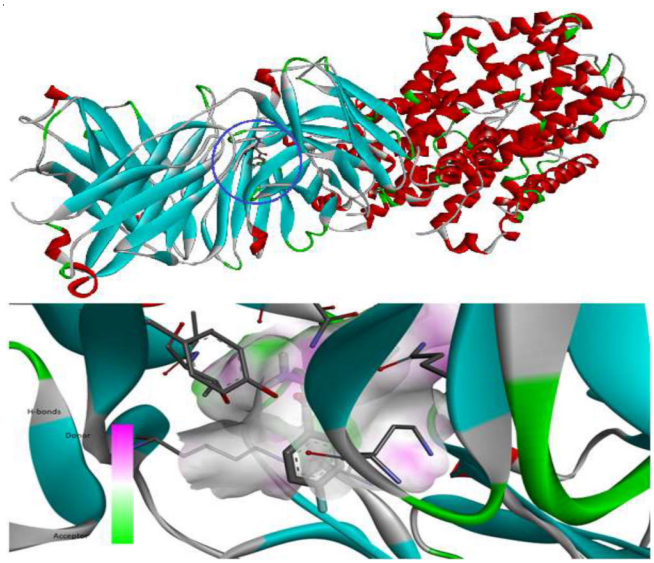

Fig. 10. The binding site and H-bonds between FMPHC and 6MOF

binding site of the title molecule. According to decreasing energy values, Table-4 ranked the drug docking poses with the protein structure. The best docking pose usually has the lowest energy. The molecule that is best docked often has lowest docking energy or vina score. The best dock pose corresponds to -7.0 kJ/mol and represents an excellent inhibition. This high vina score for the interaction between FMPHC and hNET shows that this molecule can affect the neural system up to a large extent.

TABLE-4
BINDING MODES OF FMPHC LIGAND WITH 6M0F PROTEIN

Mode	Affinity (kcal/mol)	Distance from best mode rmsd (l.b)	rmsd (u.b)
1	-7.0	0.000	0.000
2	-5.7	2.986	4.297
3	-5.6	3.432	8.675
4	-5.5	2.859	9.465
5	-5.3	6.328	11.605

Conclusion

A synthetic cathinone derivative, 4-fluoromethcathinone hydrochloride (FMPHC) was examined at a molecular level for the electronic and spectroscopic properties. The correlation between the calculated and experimental values of th structural parameters is acceptable to confirm the reliability of the calculations. Calculated vibrational wavenumbers for the optimized geometry give no negative values confirming the stable structure. The potential energy distribution (PED) has quantitatively interpreted all the vibrational bands. MEP map has clearly indicated that the negative potential site lies over Cl33 and O13 atoms, while the region around N16 has the highest positive potential. These regions are preferred sites for electrophilic and nucleophilic attack respectively. Detailed analysis of intra- and intermolecular interactions have been done using NBO and Hirshfeld surface analysis, respectively. Hirshfeld surface analysis for the title compound showed that the main contribution of inter-contacts to the Hirshfeld surfaces is coming from H-H (48.6%) and HCl/Cl-H (13.2%). The molecular docking of FMPHC ligand revealed that a strong inhibition interaction exists between the titled ligand and a model human norepinephrine transporter (hNET). The best dock pose corresponds to -7.0 kJ/mol, which shows that this molecule can affect the neural system up to a large extent.

ACKNOWLEDGEMENTS

The authors acknowledge to the Department of Physics, Chaudhary Charan Singh University, Meerut for providing the computational resources. The authors further acknowledge Prof. Sangeeta Shukla, Vice-Chancellor, Chaudhary Charan Singh University, Meerut for her support and encouragement.

CONFLICT OF INTEREST

The authors declare that there is no conflict of interests regarding the publication of this article.

REFERENCES

1. M.H. Baumann, E. Solis Jr., L.R. Watterson, J.A. Marusich, W.E. Fantegrossi and J.L. Wiley, *J. Neurosci.*, **34**, 15150 (2014); https://doi.org/10.1523/JNEUROSCI.3223-14.2014
2. J.P. Kelly, *Drug Test. Anal.*, **3**, 439 (2011); https://doi.org/10.1002/dta.313
3. A. Al-Motarreb, K. Baker and K.J. Broadley, *Phytother. Res.*, **16**, 403 (2002); https://doi.org/10.1002/ptr.1106
4. T.A. Dal Cason, R. Young and R.A. Glennon, *Pharmacol. Biochem. Behav.*, **58**, 1109 (2011); https://doi.org/10.1016/S0091-3057(97)00323-7
5. L. Poyatos, A. Torres, E. Papaseit, C. Pérez-Mañá, M. Núñez-Montero, O. Hladun, G. de la Rosa, M. Torrens, D. Fuster, R. Muga and M. Farré, *J. Clin. Med.*, **11**, 1004 (2022); https://doi.org/10.3390/jcm11041004
6. A.S. Kristensen, J. Andersen, T.N. Jørgensen, L. Sørensen, J. Eriksen, C.J. Loland, K. Strømgaard and U. Gether, *Pharmacol. Rev.*, **63**, 585 (2011); https://doi.org/10.1124/pr.108.000869
7. G.E. Torres, R.R. Gainetdinov and M.G. Caron, *Nat. Rev. Neurosci.*, **4**, 13 (2003); https://doi.org/10.1038/nrn1008
8. T. Pacholczyk, R.D. Blakely and S.G. Amara, *Nature*, **350**, 350 (1991); https://doi.org/10.1038/350350a0
9. R.A. Sansone and L.A. Sansone, *Psychiatry*, **6**, 19 (2009).
10. Synthetic Cathinones, Drug Facts Report of National Institute on Drug Abuse; National Institutes of Health, U.S. Department of Health and Human Services (2020).
11. M. Rojkiewicz, P. Kus, J. Kusz and M. Ksiazek, *Forensic Toxicol.*, **36**, 141 (2018); https://doi.org/10.1007/s11419-017-0393-6
12. https://www.euda.europa.eu/publications/drug-profiles/synthetic-cathinones_en
13. M.J. Frisch, G.W. Trucks, H.B. Schlegel, G.E. Scuseria, M.A. Robb and J.R. Cheeseman, Gaussian 09, C3 Revision B.01, Gaussian, Inc, Wallingford CT (2010).
14. C. Lee, W. Yang and R.G. Parr, *Phys. Rev. B Condens. Matter*, **37**, 785 (1988); https://doi.org/10.1103/PhysRevB.37.785
15. R. Dennington, T. Keith and J. Milam, GaussView, Semichem Inc., Shawnee Mission KS Version 5 (2009).
16. J.M.L. Martin and C.V. Alsenoy, Gar2ped, University of Antwerp (1995).
17. P. Pulay, G. Fogarasi, F. Pang and J.E. Boggs, *J. Am. Chem. Soc.*, **101**, 2550 (1979); https://doi.org/10.1021/ja00504a009
18. M.J. Turner, J.J. McKinnon, S.K. Wolff, D.J. Grimwood, P.R. Spackman, D. Jayatilaka and M.A. Spackman, CrystalExplorer 17.5. The University of Western Australia (2017).
19. O. Trott and A.J. Olson, *J. Comput. Chem.*, **31**, 455 (2010); https://doi.org/10.1002/jcc.21334
20. W.L. DeLano, The PyMOL Molecular Graphics System, Schrödinger LLC (2002).
21. D. Studio, 4.5 Guide, San Diego, CA: Accelrys Inc., (2009); http://www.accelrys.com
22. D.E. Hibbs, J. Overgaard, J.A. Platts, M.P. Waller and M.B. Hursthouse, *J. Phys. Chem. B*, **108**, 3663 (2004); https://doi.org/10.1021/jp037700l
23. S. Gunasekaran, R.A. Balaji, S. Kumeresan, G. Anand and S. Srinivasan, *Can. J. Anal. Sci. Spectrosc.*, **53**, 149 (2008).
24. T.A. Yousef, G.M. Abu El-Reash and R.M. El Morshedy, *Polyhedron*, **45**, 71 (2012); https://doi.org/10.1016/j.poly.2012.07.041
25. B.H. Stuart, Infrared Spectroscopy: Fundamentals and Applications, John Willey & Sons (2004).
26. V.K. Rastogi, M.A. Palafox, R.P. Tanwar and L. Mittal, *Spectrochim. Acta A Mol. Biomol. Spectrosc.*, **58A**, 1987 (2002); https://doi.org/10.1016/S1386-1425(01)00650-3
27. C. Wu, W. Xie, L. Li, W. Li, J. Wang and T. Sun, *J. Mol. Struct.*, **1175**, 638 (2019); https://doi.org/10.1016/j.molstruc.2018.08.035
28. M.A. Spackman and D. Jayatilaka, *CrystEngComm*, **11**, 19 (2009); https://doi.org/10.1039/B818330A
29. Y.F. Baba, Y. Sert, Y.K. Rodi, S. Hayani, J.T. Mague, D. Prim, J. Marrot, F.O. Chahdi, N.K. Sebbar and E.M. Essassi, *J. Mol. Struct.*, **1188**, 255 (2019); https://doi.org/10.1016/j.molstruc.2019.03.103
30. A. Schlessinger, E. Geier, H. Fan, J.J. Irwin, B.K. Shoichet, K.M. Giacomini and A. Sali, *Proc. Natl. Acad. Sci. USA*, **108**, 15810 (2011); https://doi.org/10.1073/pnas.1106030108